UPPSALA
UNIVERSITET

DiVA

http://uu.diva-portal.org

Reactively sputtered ZrN for application as reflecting back contact in CIGS solar cells

Sebastian Schleussner[a,*], Tomáš Kubart[a], Tobias Törndahl[a], Marika Edoff[a]

[a]Solid State Electronics, Uppsala University, P.O. Box 534, SE-75121 Uppsala, Sweden.
Tel.: +46184713113; Fax: +4618555095.

Abstract

We investigate reactively sputtered films of zirconium nitride, ZrN, for use as highly reflecting back contacts in Cu(In,Ga)Se$_2$ (CIGS) devices with sub-micrometer absorbers. We identify the nitrogen flow and the sputter current as the decisive parameters for the composition, and demonstrate a method for determining the nitrogen flow at which the transition from metallic to compound sputtering mode occurs for a given current. Films prepared at this working point consist of stoichiometric ZrN with a low resistivity, a high reflectance for red and infrared light, and have a fairly high sputter rate. Calculations show that the reflectance at the ZrN/CIGS interface is significantly superior to that at the standard Mo/CIGS interface.

Keywords: ZrN, Reactive DC magnetron sputtering, Optical Properties, CIGS

1. Introduction

With competition in the photovoltaics market growing steadily, using a thinner absorbing layer in solar cells becomes more and more attractive. A general economic benefit is that material costs are reduced this way; for thin-film solar cells, it usually also translates into shorter processing times for each device and thereby into higher production throughput. However, such a reduction is practically limited to around the thickness at which the absorber material starts being transparent to a significant degree even above its band-gap energy. The problem is illustrated for thin-film solar cells based on Cu(In,Ga)Se$_2$ (CIGS) in Figure 1, which shows the external quantum efficiency characteristics of one conventional CIGS solar cell with a typical absorber thickness (1.7 µm) and of one with a thin absorber (0.5 µm). It can be seen that while the bandgap of both absorbers is virtually identical, the cell with a 0.5 µm absorber has considerable losses compared to the standard cell, which can be attributed at least partly to absorption losses.

The limitation caused by reduced absorption can be alleviated by increasing the effective length of the optical path. Approaches for this include light trapping by means of rough or textured interfaces [1, 2] and increasing the reflectance at the backside of the absorber by replacing the traditional molybdenum back contact with a more reflective layer [3]. We have previously suggested using zirconium nitride (ZrN) as such a back-reflector layer [4]. ZrN has been investigated for application as transparent heat mirrors because of its high long-wavelength reflectance [5] and is also known for its high corrosion resistance [6].

The present work investigates stoichiometric and non-stoichiometric zirconium-nitride (ZrN$_x$) films prepared on glass by reactive DC magnetron sputtering, which is one of the most common methods. With some literature on sputtered ZrN considering the nitrogen flow [7, 8, 9] and others considering the *ratio* of nitrogen to argon flow [10, 11], it is not entirely obvious which of these parameters has the most direct influence when sputtering ZrN. We therefore begin with an experiment to examine this question. Subsequently, we analyse the sputter rate and the material properties reflectance, resistivity, composition and structure of these ZrN$_x$ films. These analyses allow us to correlate the properties of interest for the application in solar cells with more certain process conditions: Besides a high film reflectance, a high sputter rate is desirable for achieving high process througput and minimizing inclusion of residual oxygen into films. Since the ZrN$_x$ films are to be used as a part of the electrical back contact, their resistivity should also be low.

---

*Corresponding author.
Email address: sebastian.schleussner@angstrom.uu.se (Sebastian Schleussner)
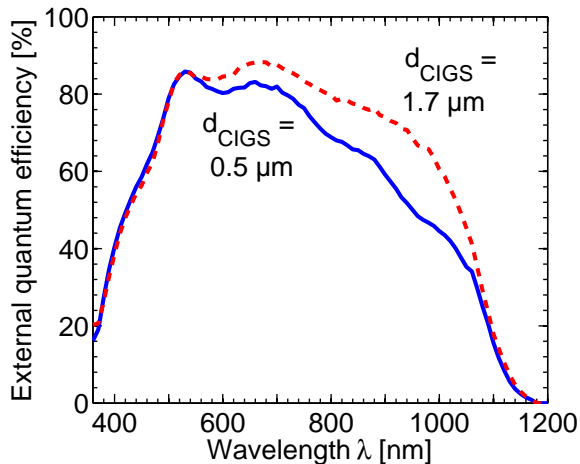
Figure 1: External quantum efficiency of a CIGS solar cell with standard thickness (1.7 μm, dashed line) and of one with a thin absorber (0.5 μm, solid line).

2. Experimental

Zirconium nitride (ZrN) films have been deposited by DC magnetron sputtering in a *von Ardenne CS 730S* high-vacuum system, where a turbomolecular pump with a nominal pumping speed of 880 l/s provided a base pressure of 1×10^{-7} Torr or below. The pump was not throttled throughout the experimental series, which yielded an effective pumping speed of approximately 425 l/s under process conditions. An *ENI RPG-50* plasma generator was used in continuous-DC mode with current control, acting on a magnetron with a 99.2 % pure zirconium target of 150 mm diameter, which was mounted at a distance of 55 mm from the sample plane.

Samples were loaded onto the process chamber's rotary table via a load-lock system, in batches of four. Each of the samples investigated here was a 1 mm thick sheet of soda-lime glass of the dimensions 50×100 mm². A piece of microscopy cover glass usually shaded a small part of each sample to provide a step for subsequent thickness measurements. The samples and sample mounting were electrically floating (that is to say, without either grounding or biasing), and no external heating was applied.

The target was sputter-cleaned for five minutes at a current of 3 A and an argon gas flow of 100 standard cubic centimeters per minute (sccm). The fabrication of each ZrN layer was then initialized by a conditioning of the target in a mixed argon-nitrogen atmosphere with the intended nitrogen flow, followed by the deposition on the sample. For the process the argon flow was reduced in proportion to the nitrogen flow in order to minimize changes of the pressure.

Samples were fabricated under various conditions, with currents between 3 A and 6 A and nitrogen flows ranging from 0 sccm to 40 sccm. This paper focuses on four of these samples, prepared at a current of 3 A within a wide range of nitrogen flows, denoted **I** through **IV**. The relevant process parameters for these samples are summarized in Table 1. The crystal structure of the sputtered films was characterized by grazing-incidence (GI-XRD) and Θ–2Θ X-ray diffraction (T2T-XRD) scans in a *Philips X'pert MRD* equipped with an X-ray mirror and a parallel-plate collimator, using Cu-K$_\alpha$ radiation. All GI-XRD diffractograms were collected at an angle of incidence of 0.5°. The areal density of Zr atoms was determined from X-ray fluorescence performed in a *Spectro X-lab 2000* and calibrated with *Dektak Gamma step* profilometer measurements on several samples, which it fitted well; the accuracy of this measurement is estimated to be in the order of 10 nm.

Elemental depth profiles of the thin films were measured using time-of-flight energy elastic recoil detection analysis (ToF-E ERDA) [12] with 40 MeV ^{127}I^{9+} ions as projectiles. The measurements were performed at the Tandem Laboratory, Uppsala University. The incident angle of primary ions and the exit angle of recoils were both 67.5° to the sample surface normal, giving a recoil angle of 45°. A detailed description of the experimental setup has been given by Zhang *et al.* [13]. All recoil ToF-E ERDA spectra were analysed using the CONTES code [14] for extracting the depth profiles of relative elemental concentration. The measurement error is estimated to be in the order of 6 % of the elemental ratio value.

Specular reflectance was analysed at near-normal incidence in a single-beam spectrophotometer at Uppsala University, which is described in detail by Nostell *et al.* [15]. The spectra considered here were recorded in steps of 10 nm in the wavelength range of 300 nm to 1100 nm, since this covers most of the optically active range of CIGS solar cells.

3. Optics

While the reflectance characteristics are measured in air, the most relevant property for assessing the reflector material is its reflectance within the solar-cell device. This can be calculated based on the following considerations:

On the one hand, the reflectance at the interface between any two (nonmagnetic) materials is governed by the Fresnel formula [16, ch 3.1.4]

$$R(\omega) = \frac{|\underline{N}_1(\omega) - \underline{N}_2(\omega)|^2}{|\underline{N}_1(\omega) + \underline{N}_2(\omega)|^2}, \qquad (1)$$

Table 1: Process parameters for the samples **I**–**IV** discussed in this paper. Q_N and Q_{Ar} are the nitrogen and argon flows, p is the process pressure and U is the target voltage. The sputter current was I = 3 A for all four samples, the process duration was 180 s.

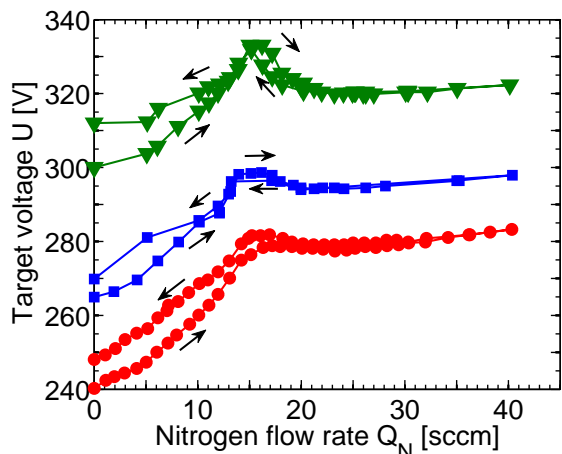| Sample	Q_N [sccm]	Q_{Ar} [sccm]	p [mTorr]	U [V]	Rate [nm/s]
I	4	97	3.30	232	2.2
II	8	95	3.32	252	1.4
III	20	87	2.88	261	0.7
IV	36	76	3.00	273	0.5

Figure 2: Target voltage as a function of nitrogen flow, for sputter current $I = 5\,\mathrm{A}$ and various argon flows: Discs $Q_{Ar} = 100\,\mathrm{sccm}$, squares $75\,\mathrm{sccm}$, triangles $50\,\mathrm{sccm}$. Arrows to the right and left indicate the branches for increasing and decreasing nitrogen flow, respectively.

where $\underline{N}_i$ are the complex refractive indices of the two materials,

$$\underline{N} = n - jk = \sqrt{\underline{\varepsilon}} \qquad (2)$$

with the real part of the refractive index n, the extinction coefficient k and the complex dielectric function ε. For the refractive index of $CuIn_{0.77}Ga_{0.23}Se_2$ we use data from Orgassa *et al.* [3, App. B], and data from the CRC Handbook [17, Section 12] is used for molybdenum.

On the other hand, it is known since earlier that zirconium nitride can be viewed as a Drude free-electron metal [5, 8], for which the complex dielectric function $\underline{\varepsilon}_r$ for visible and infrared radiation is given by the relation

$$\varepsilon_r(\omega) = \varepsilon_\infty - \frac{\omega_P^2}{\omega^2 + i\omega/\tau}, \qquad (3)$$

with the high-frequency dielectric constant ε_∞, the plasma frequency ω_P and the electron scattering time τ. The dielectric function of zirconium-nitride films can thus be determined by fitting Eq. 3 to the measured reflectance data via Eqs. 1 and 2 (setting $\underline{N}_1 = n = 1$ for air).

4. Reactive Sputter Process

For reactive sputtering, a reactive gas is added to the conventional argon working atmosphere. In the general case, the control of a reactive sputter process is complicated by the existence of a hysteresis effect with respect to the flow of the reactive gas. The hysteresis effect limits the achievable compositions or decreases the deposition rate substantially. In a typical process, two distinct operating modes exist: When the flow of reactive gas is low, the target surface is kept metallic and the deposition rate is high, but the deposited films are under-stoichiometric. For higher reactive-gas flows, the target gets covered with a compound due to the reaction with reactive gas, which results in a low deposition rate. The hysteresis can be suppressed if the pumping speed is sufficiently high [18], so that one can explore the whole area of compositions and working conditions.

As laid out by Lieberman and Lichtenberg [19, Ch. 14.5], steady-state sputtering operation requires that the number of ion particles in the plasma be constant. Ions are generated in a cascade process, where impinging ions cause the emission of *secondary electrons* from the target with a emission coefficient γ, which in turn create N new ion-electron pairs in the plasma. The steady-state condition can thus be described by the relation $N \cdot \gamma = 1$. N is approximately proportional to the target voltage U and increases with increasing pressure. The pressure dependence can be attributed to the reduction of the mean free path of electrons with increasing pressure, which in turn enhances the probability of ionizing a gas atom. The emission coefficient γ is primarily dependent on the target material, and like the sputter rate it is usually lower for compounds than for metals.

Rewriting the steady-state condition as $N^* \gamma \cdot U = 1$, where N^* is the voltage-independent part of N and of the dimension V^{-1}, indicates that the target voltage can be used as a measure of the target state in reactive sputtering processes. As Sproul *et al.* indicate [20], the transition from metallic mode to compound mode is indicated by a local extremum of the voltage as a function of the reactive gas flow.

5. Results and Discussion

The link between target state and target voltage was used to verify the dependence of the sputter mode on process conditions. For this, the nitrogen flow Q_N was increased in steps over a range from $0\,\mathrm{sccm}$ to $40\,\mathrm{sccm}$ and decreased again, at various sputter currents and argon flows. Figure 2 displays the target voltage recorded for each step at a current of $5\,\mathrm{A}$, for argon flows between $50\,\mathrm{sccm}$ and $100\,\mathrm{sccm}$. Qualitatively the characteristics are quite similar to each other. The main difference between them lies in the decrease of the voltage level with increasing argon flows, which is be expected owing to the change in process pressure, which was roughly proportional to the change in flows. Most importantly, however, it can be seen that the position of the local maximum with respect to Q_N is practically independent of the argon flow. This shows that the compound-mode working point for a given current is indeed only determined by the nitrogen flow Q_N, which agrees well with the sputter-process model presented by Berg and Nyberg [21]. Moreover, no signs of the hysteresis effect are visible in the characteristics, which indicates that the pumping speed is sufficiently high in the sense noted in Section 4. Different sputter currents in the range from $2.5\,\mathrm{A}$ to $6\,\mathrm{A}$ yielded similar characteristics. The position of the local maxima
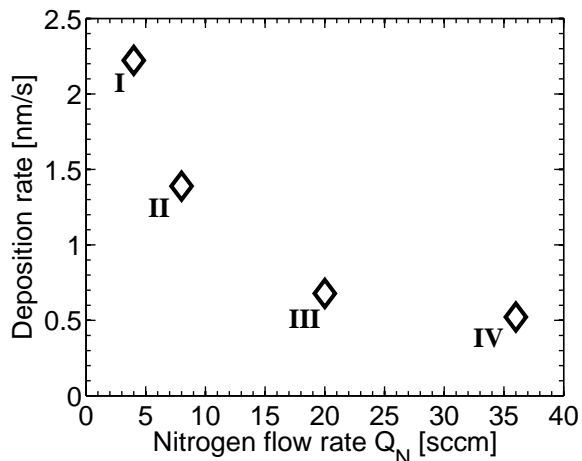
Figure 3: Deposition rate as a function of nitrogen flow, for the sputter current $I = 3\,\mathrm{A}$. The Roman numbers correspond to the samples listed in Table 1.
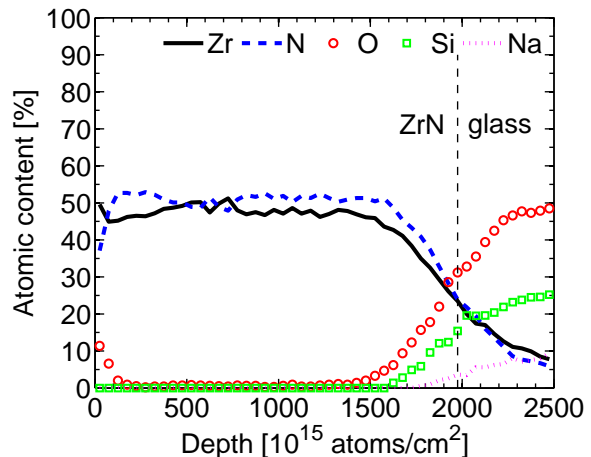

Figure 4: ERDA atomic-content profiles of the elements Zr, N, O, Si, and Na in sample **II**. The x-axis unit of $1 \times 10^{15}\,\mathrm{atoms/cm^2}$ corresponds to one monolayer. The increase of the O signal near 0 hints at surface oxidation. The dashed vertical line marks the actual border between the film and the glass, which is smeared out in the data due to the limited depth resolution of ERDA. The Zr and N signals are fairly uniform and close to a ratio of 1.

scaled with the current and could be fitted well by the linear relation

$$Q_N^* = 4 \cdot (I - 1) \qquad (4)$$

where Q_N^* is given in sccm and I is given in A. Therefore we consider the current and the nitrogen flow as the main process parameters in the following experiments.

As shown in Figure 3 for the samples prepared at $I = 3\,\mathrm{A}$, the deposition rate at $4\,\mathrm{sccm}$ of nitrogen flow is relatively high with a value of $2.2\,\mathrm{nm/s}$, similar to metallic sputtering of Zr, which at this current would proceed at a rate of approximately $3.5\,\mathrm{nm/s}$. The rate then drops at $8\,\mathrm{sccm}$, which is the special flow given by Eq. 4, and reaches a much lower level of about $0.5\,\mathrm{nm/s}$ at high nitrogen flows. This supports our finding that a transition from metallic to compound mode occurs at or near the flow yielding a maximum in the target voltage.

ERDA analyses were performed on samples **I** through **IV**; Figure 4 displays the ERDA depth profiles of selected elements in sample **II**. The overlap of the Zr and N signals with the O and Si signals from SiO_2 in the underlying glass is owed to the limited depth resolution of the ERDA measurement. On the other hand, we attribute the oxygen peak at the surface to oxidation due to air exposure. Apart from these regions, the zirconium and nitrogen contents in Figure 4 prove to be fairly uniform, in which they are typical for all samples measured, and close to a N/Zr ratio of $x = 1$, which is to say, close to stoichiometry. For all samples, the mean value of the N/Zr ratio has been calculated from the region of the respective profiles which does not feature significant amounts of oxygen coming from the surface or the substrate, as noted above, and these values are noted together with other properties of the samples in Table 2.

GI-XRD diffractograms of the four main samples are seen in Figure 5. For samples **II** ($Q_N = 8\,\mathrm{sccm}$) and **III** ($Q_N = 20\,\mathrm{sccm}$) the films are well crystal-

lized in the cubic (NaCl-type) ZrN phase with no secondary phases. With increasing nitrogen flows, the peaks broaden and shift towards lower diffraction angles. A similar shift of the peaks towards lower angles was also found in the T2T-XRD diffractograms, which allow an accurate calculation of the lattice constants. The increase of the lattice constant a is seen in Table 2. It seems likely that this dilatation of the crystal lattice is caused by interstitial inclusion of nitrogen, as also Benia *et al.* [7] assume.

For sample **IV** ($Q_N = 36\,\mathrm{sccm}$), the composition N/Zr ≈ 1.4 shown by ERDA would predict the structure Zr_3N_4, but the diffractogram does not indicate any crystalline Zr_3N_4. Given the high background level in the diffractogram and the width of the peaks, the sample may well consist of ZrN crystals embedded in an amorphous Zr_3N_4 matrix, again in accordance with Benia *et al.* [7].

For sample **I**, prepared at the lowest nitrogen flow of $4\,\mathrm{sccm}$, the diffractogram differs strongly from the others. In accordance with the ERDA result of N/Zr ≈ 0.2, the material largely consists of metallic zir-

Table 2: Some relevant properties of the samples **I**–**IV**. $R_{800\,\mathrm{nm}}$ stands for the specular reflectance at the wavelength $800\,\mathrm{nm}$, N/Zr describes the average atomic ratio of nitrogen to zirconium as obtained by ERDA, and a is the crystal lattice constant as obtained from T2T-XRD measurements.

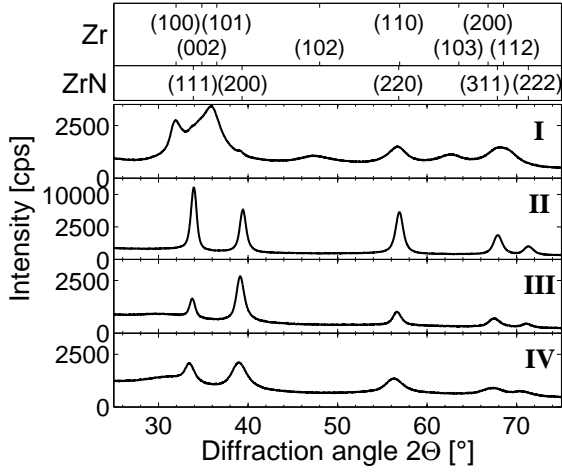| Sample	d	$R_{800\,\mathrm{nm}}$	N/Zr	a	Colour
	[nm]	[%]	(x)	[Å]	
I	400	60	0.22	-	silver
II	250	78	1.07	4.60	golden
III	120	39	1.20	4.63	dark golden
IV	100	65	1.37	4.66	grey-brown

Figure 5: Grazing-incidence XRD patterns. The two topmost boxes denote the positions of the relevant Zr and ZrN reflections; the Roman numbers in the main figure correspond to the samples listed in Table 1.
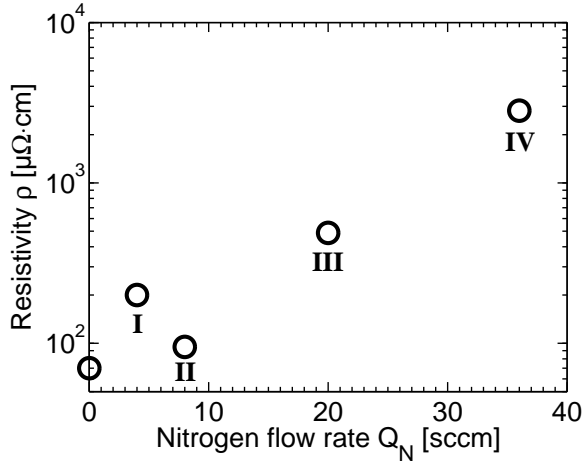

Figure 6: Electrical resistivity as a function of nitrogen flow. The Roman numbers correspond to the samples listed in Table 1.

Figure 7: Specular reflectance at near-normal incidence. The Roman numbers correspond to the samples listed in Table 1.

conium, as witnessed by the dominating reflections of the hexagonal Zr phase, with traces of reflections of the cubic ZrN phase at the ZrN-(111) and (200) positions.

The dependence of the film resistivity on the nitrogen flow is seen in Figure 6. A minimum of the resistivity can be seen at the presumed point of stoichiometry, for sample **II**, and this fits the finding of Benia *et al.* [8]. The higher resistivity for sample **I** is consistent with the indications that this film is mainly made up of metallic zirconium with nitrogen dissolved in it, since the nitrogen atoms may act as scattering centres for electrons within the metal lattice. Likewise, the rise in resistivity from sample **II** suggests that in sample **III** additional nitrogen atoms are trapped in the ZrN matrix, working in a similar manner as before, while the further strong increase in resistivity towards sample **IV** is consistent with the compositional and structural indications for the likely presence of the insulating Zr_3N_4 phase in that sample.
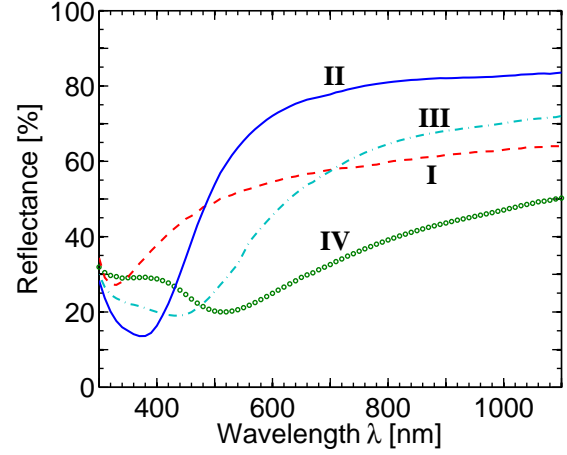
Figure 7 shows the spectral reflectance of the four samples. Samples **II** and **III** clearly display the characteristics of a free-electron metal as described by the Drude model, with a high reflectance plateau at long wavelengths and a minimum in the blue to ultraviolet regime. Sample **II** achieves the highest and most stable long-wavelength reflectance, which in accordance with literature once more identifies it as stoichiometric [5, 8]. Compositional deviation to substoichiometry in sample **I** yields characteristics similar to metallic zirconium, with an infrared reflectance in the order of 60 % and a much weaker reflectance reduction at short wavelengths. Deviation towards over-stoichiometry in sample **III** also diminishes the long-wavelength reflectance but shifts the onset of the high-reflectance regime towards longer wavelengths. Far above stoichiometry, in sample **IV**, the trends in the onset and above all level of this regime continue, with the reflectance reaching no more than 50% within the considered wavelength interval.

Samples were also prepared with the sputter currents $I = 4\,A$, $5\,A$ and $6\,A$, at the nitrogen flows given by Eq. 4. The results show that the highest long-wavelength reflectance achieved is fairly independent of the sputter current. Also, the nitrogen flows yielding the highest reflectance again obey the relation in Eq. 4, and small deviations from the optimal nitrogen flow do not cause dramatic drops in the long-wavelength reflectance.

For all four samples **I** through **IV**, the reflectance characteristics could be fitted, for wavelengths above their respective reflectance minimum, by the Drude model as presented in Section 3. The resulting parameters ε_∞, ω_P and $1/\tau$ are compiled in Table 3, and Figure 8 shows the real part n and imaginary part k of the complex refractive index of sample **II** as an example.

Figure 9 demonstrates the resulting reflectance that may be expected at the back contact, for the case of ZrN contacts constituted by the conductive samples **I** through **III** and for a standard molybde-
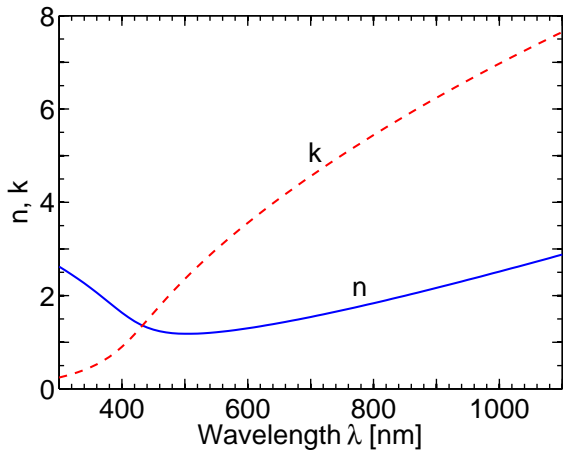
Figure 8: Real part n and imaginary part k of the complex refractive index of the stoichiometric sample **II**.
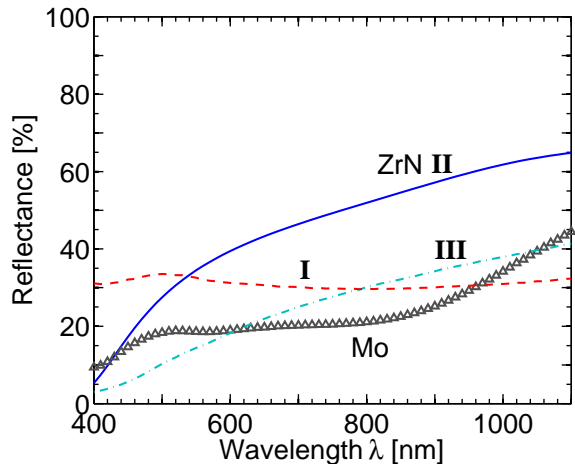

Figure 9: Simulated reflectance at several ZrN/CIGS interfaces, compared to a standard Mo/CIGS interface.

num contact. The data have been calculated by applying Eq. 1 to the n and k values of CIGS and of the respective back-contact material. It is evident that the back-contact reflectance is considerably enhanced over virtually all of the relevant part of the solar spectrum. On average, the optical losses in this part of the stack are reduced by over a third for wavelengths over 600 nm.

6. Conclusion

We have identified the nitrogen flow and the sputter current as the decisive parameters for the composition of reactively sputtered zirconium nitride, and we have demonstrated a method for determining the nitrogen flow at which the transition from metallic to compound sputtering mode occurs for a given current, by plotting the target bias over the nitrogen flow. Further analyses have shown that films prepared at this working point consist of stoichiometric ZrN, which proves to have properties interesting for for solar-cell reflectors, namely a relatively low resistivity, a high reflectance for red and infrared light, and a fairly high sputter rate. Simple optical modelling of the interface between a CIGS absorber and different back contacts shows that the reflectance of this stoichiometric zirconium nitride exceeds that of the usual molybdenum and thus can contribute to reducing the optical losses in very thin solar-cell devices. Strongly under- and over-stoichiometric zirconium-nitride films do not share these properties and are thus uninteresting for the considered application.

Table 3: Drude-model parameters.

Sample	ε_∞	$\hbar\,\omega_P$ [eV]	$\hbar/\tau$ [eV]
Zr	1.7	6.7	1.7
I	1.7	7.0	1.9
II	13.6	10.9	0.8
III	12.1	8.9	1.1
IV	8.0	6.7	2.0

References

[1] R. Brendel, D. Scholten, Modeling light trapping and electronic transport of waffle-shaped crystalline thin-film Si solar cells, Applied Physics A: Materials Science & Processing 69 (2) (1999) 201–213. `doi:10.1007/s003390050991`.

[2] J. Müller, O. Kluth, S. Wieder, H. Siekmann, G. Schöpe, W. Reetz, O. Vetterl, D. Lundszien, A. Lambertz, F. Finger, B. Rech, H. Wagner, Development of highly efficient thin film silicon solar cells on texture-etched zinc oxide-coated glass substrates, Solar Energy Materials and Solar Cells 66 (1-4) (2001) 275–281. `doi:10.1016/S0927-0248(00)00184-7`.

[3] K. Orgassa, H. W. Schock, J. H. Werner, Alternative back contact materials for thin film Cu(In,Ga)Se$_2$ solar cells, Thin Solid Films 431-432 (2003) 387–391. `doi:10.1016/S0040-6090(03)00257-8`.

[4] J. Malmström, S. Schleussner, L. Stolt, Enhanced back reflectance and quantum efficiency in Cu(In,Ga)Se$_2$ thin film solar cells with a ZrN back reflector, Appl. Phys. Lett. 85 (13) (2004) 2634–6. `doi:10.1063/1.1794860`.

[5] M. Veszelei, K. E. Andersson, C.-G. Ribbing, K. Järrendahl, H. Arwin, Optical constants and drude analysis of sputtered zirconium nitride films, Applied Optics 33 (10) (1994) 1993. `doi:10.1364/AO.33.001993`.

[6] L. E. Toth, Transition metal carbides and nitrides, Academic press, 1971.

[7] H. M. Benia, M. Guemmaz, G. Schmerber, A. Mosser, J.-C. Parlebas, Investigations on non-stoichiometric zirconium nitrides, Applied Surface Science 200 (2002) 231–238. `doi:10.1016/s0169-4332(02)00925-x`.

[8] H. M. Benia, M. Guemmaz, G. Schmerber, A. Mosser, J.-C. Parlebas, Optical and electrical properties of sputtered ZrN compounds, Catalysis Today 89 (3) (2004) 307–312. `doi:10.1016/j.cattod.2003.12.006`.

[9] D. Pilloud, A. S. Dehlinger, J. F. Pierson, A. Roman, L. Pichon, Reactively sputtered zirconium nitride coatings: structural, mechanical, optical and electrical characteristics, Surface and Coatings Technology 174-175 (2003) 338–344. `doi:10.1016/S0257-8972(03)00613-3`.

[10] L. Hu, D. Li, G. Fang, Influence of N$_2$:(N$_2$+Ar) flow ratio and substrate temperature on the properties of zirconium nitride films prepared by reactive dc magnetron sputtering, Applied Surface Science 220 (2003) 367–371. `doi:10.1016/s0169-4332(03)00843-2`.

[11] J. S. Jeng, S. H. Wang, J. S. Chen, Effects of substrate bias and nitrogen flow ratio on the resistivity and crystal structure of reactively sputtered ZrN$_x$ films at elevated temperature, Journal of Vacuum Science & Technology A: Vacuum, Surfaces, and Films 25 (4) (2007) 651–658. `doi:10.1116/1.2735966`.

[12] J. R. Tesmer, M. Nastasi, Handbook of Modern Ion Beam Materials Analysis, Materials Research Society, Pittsburgh, 1995.

[13] Y. Zhang, H. J. Whitlow, T. Winzell, I. F. Bubb, T. Sajavaara, K. Arstila, J. Keinonen, Detection efficiency of time-of-flight energy elastic recoil detection analysis systems, Nuclear Instruments and Methods in Physics Research Section B: Beam Interactions with Materials and Atoms 149 (4) (1999) 477–489. `doi:10.1016/S0168-583X(98)00963-X`.

[14] M. S. Janson, Contes instruction manual (internal report), Tech. rep., Uppsala (2004).

[15] P. Nostell, A. Roos, D. Rönnow, Single-beam integrating sphere spectrophotometer for reflectance and transmittance measurements versus angle of incidence in the solar wavelength range on diffuse and specular samples, Review of Scientific Instruments 70 (5) (1999) 2481. `doi:10.1063/1.1149781`.

[16] C. F. Klingshirn, Semiconductor Optics, Springer, Berlin, 1997.

[17] D. R. Lide, CRC Handbook of Chemistry and Physics, 88th Edition, CRC Press, Boca Raton, FL, 2007.
URL `http://www.hbcpnetbase.com/`

[18] S. Kadlec, J. Musil, J. Vyskocil, Influence of the pumping speed on the hysteresis effect in the reactive sputtering of thin films, Vacuum 37 (10) (1987) 729–738. `doi:10.1016/0042-207X(87)90262-4`.

[19] M. A. Lieberman, A. J. Lichtenberg, Principles of Plasma Discharges and Materials Processing, 2nd Edition, Wiley Interscience, 2005.

[20] W. Sproul, D. Christie, D. Carter, Control of reactive sputtering processes, Thin Solid Films 491 (1-2) (2005) 1–17. `doi:10.1016/j.tsf.2005.05.022`.

[21] S. Berg, T. Nyberg, Fundamental understanding and modeling of reactive sputtering processes, Thin Solid Films 476 (2) (2005) 215–230. `doi:10.1016/j.tsf.2004.10.051`.